RESEARCH ARTICLE

Mechanics-Based Drill Bit Design for Soil Sampling in Resource Exploration

Ziming Chen[1], Hongyuan Zhang[2], Hongfei Hou[1], Wang Han[1], Pan Zhang[1], Wushuai Wang[1], Chen Zhao[1,*] and Qirui Li[1]

[1] School of Mechanical Engineering, Yanshan University, Qinhuangdao 066004, China
[2] Hebei Special Equipment Supervision and Inspection Institute, Shijiazhuang 050061, China

Abstract

To meet the requirements for automated sampling of silty clay and loam in mineral exploration, a soil-sampling drill bit was designed, and its structural parameters, soil-cutting mechanism, and drilling performance were investigated. Based on the characteristics of helical soil conveying, the helix angle of the flight was set to 14°, giving a pitch of approximately 35 mm. Building on the McKyes-Ali model, the soil failure surface was represented as a composite surface consisting of a planar surface and a logarithmic spiral surface, and the cutting zone was divided into a central failure zone and two lateral failure zones. The calculated total cutting resistance of the drill bit was lowest at a rake angle of 18°, while the lateral resistance accounted for 30%–40% of the total cutting load. A coupled RecurDyn-EDEM model of the drill bit-soil interaction was then established using the Hertz-Mindlin with JKRV2 contact model. Thirteen numerical tests were conducted to investigate the effects of rotational speed and feed speed on thrust force and torque. Both thrust force and torque increased markedly with increasing feed speed. Increasing the rotational speed appropriately while limiting the feed speed reduced the drilling load. Field sampling tests in silty clay were then carried out at depths of 5–30 cm. Twelve sampling operations were completed, of which eleven yielded samples weighing at least 200 g.

Keywords: soil-sampling drill bit, soil sampling, three-dimensional cutting model, coupled simulation.

1 Introduction

In mineral exploration, the acquisition of geological samples is a critical step. Conventional soil-sampling methods are often inefficient, labor-intensive, difficult to perform accurately, and strongly dependent on environmental conditions. During emergency inspections, particularly in areas affected by environmental contamination or other hazards, rapid soil sampling is essential for identifying pollution sources, assessing contaminant dispersion, and supporting emergency response, whereas manual sampling may expose personnel to substantial safety risks.

Submitted: 21 September 2026
Revised: 17 October 2026
Accepted: 20 October 2026
Published: 27 November 2026

Vol. 1, **No.** 1, 2026.
10.62762/JER.2026.773413

***Corresponding author:**
✉ Chen Zhao
zhaochen@ysu.edu.cn

Citation
Chen, Z., Zhang, H., Hou, H., Han, W., Zhang, P., Wang, W., Zhao, C., & Li, Q. (2026). Mechanics-Based Drill Bit Design for Soil Sampling in Resource Exploration. *Journal of Energy and Resources*, 1(1), 5-19.

© 2026 by the Authors. Published by Institute of Central Computation and Knowledge. This is an open access article under the CC BY license (https://creativecommons.org/licenses/by/4.0/).

Under these application scenarios, soil-sampling equipment must collect representative samples at predetermined depths, control the boundaries of the sampling layer, minimize sample disturbance, obtain a sufficient sample mass in each operation, run continuously, and keep the operator safe. Standards have established requirements for soil-sampling procedures. Studies on autonomous soil sampling with ground robots further indicate that traversing complex terrain, autonomously selecting sampling locations, and coordinating sampling and analysis remain key challenges for fully unmanned operation [1].

Research on soil-sampling devices began relatively early outside China, with initial efforts focusing on reducing the resistance during sampler insertion and withdrawal, preserving the structure of undisturbed soil samples, and improving the efficiency of single-operator sampling. Harper [2] reduced sampling friction in wet soil by installing ribs on both sides of the sampling tube and reinforcing the collar and cutting edge. Groenewoud [3] developed a threaded, guided soil sampler for collecting undisturbed forest-soil samples. Walker et al. [4] developed a precision soil sampler, while Karahashi et al. [5] designed a powered coring device consisting of a motor and tripod to counteract the reaction forces generated during drilling. These studies laid the foundation for powered sampling, resistance-reduction strategies, and low-disturbance sampler design. For stratified sampling based on auger drilling, the compatibility between soil cutting and helical conveying must be clarified so that the drill bit balances drilling resistance and soil-conveying capacity.

Powered, vehicle-mounted, and automated soil-sampling systems followed [6]. Burrage et al. [7] coupled a powered sampling mechanism to an agricultural tractor, enabling rapid soil sampling by a single operator. Hubers [8] proposed a vehicle-mounted soil sampler. Sibley et al. [9] developed an on-the-go soil-sampling system that collects samples of controlled quantity for soil nitrate-nitrogen mapping. Fiechter [10] integrated a probe, drilling device, and mechanisms for sample collection, labeling, and storage into an autonomous mobile platform. These systems progressively allowed site-specific operation, samples of controlled quantity, and association of samples with spatial and operational information.

Later work moved toward hydraulic and electro-pneumatic sampling units. Baarstad et al. [11] used a hydraulic sampler to limit plot disruption, Kornecki et al. [12] extracted soil cores with a hydraulic cutting device, and Yildirim et al. [13] evaluated an electro-pneumatic sampling method for real-time soil sensing. Overall, sampling equipment has gradually evolved from mechanically assisted operation toward coordinated integration of positioning, control, and sampling execution. However, for the soil types and depth range considered in this study, positioning and control must be combined with the cutting, soil-conveying, and force characteristics of the drill bit to determine suitable structural parameters and drilling conditions.

In summary, existing studies cover handheld, powered, vehicle-mounted, and autonomous soil-sampling equipment, but most research has focused on power supply, mobile platforms, positioning and control, and sample-collection procedures. For automated stratified sampling of silty clay and loam at depths of 10–30 cm, relatively little attention has been paid to the coordinated design of soil-conveying performance, drill-bit geometry, three-dimensional soil failure patterns, and drilling operating conditions. Some existing soil-cutting models simplify the failure surface as a single plane. When only the central failure zone directly ahead of the tool is considered, the load induced by lateral soil failure may be underestimated [14]. In addition, the coupled effects of structural parameters, rotational speed, and feed speed on axial force and torque require verification through theoretical analysis, coupled simulation, and prototype testing.

During drilling, the drill bit cuts the soil in the central region and directs it toward the surrounding area to facilitate soil transport. The helix angle and structural parameters of the drill bit affect soil-conveying performance, drilling resistance, and sampling quality, while rotational speed and feed speed determine the thrust force and torque on the bit and, jointly, the feed per revolution. Once the structural parameters are fixed, the combined effect of the two operating parameters on axial thrust and torque must therefore be investigated to select suitable operating conditions.

To meet the requirements for automated soil sampling at depths of 10–30 cm, the main structural parameters of the drill bit were first determined from the mechanisms of helical soil conveying and soil

cutting, and a three-dimensional cutting model incorporating lateral soil failure was established. A coupled RecurDyn-EDEM simulation model was then developed to investigate the effects of rotational speed and feed speed on drill-bit thrust force and torque. Finally, outdoor prototype tests were conducted to evaluate the sampling capability of the drill bit.

The remainder of this paper is organized as follows. Section 2 analyzes the helical soil-conveying mechanism, determines the structural parameters of the drill bit, and establishes a three-dimensional cutting model that accounts for lateral soil failure. Section 3 develops a RecurDyn-EDEM co-simulation model, calibrates the soil contact parameters, and investigates the effects of rotational speed and feed speed on the axial force and torque of the drill bit. Section 4 reports outdoor sampling tests in silty clay. Section 5 summarizes the main conclusions.

2 Soil-Sampling Drill Bit

2.1 Design Requirements

According to GB/T 36199-2018, *Soil Quality–Guidance on Soil Sampling Techniques*, surface contamination of the soil layer should be avoided during soil sampling; see also ISO 18400-102 [15]. The target soils in this study were primarily silty clay and loam. Soil samples were collected from depths of 10–30 cm, with each sample weighing approximately 200 g.

The soil-drilling mechanism consists of a drive assembly, a transmission assembly, and a drilling assembly, and moves vertically along a guide rail under the actuation of the guiding mechanism. A schematic diagram is shown in Figure 1. Based on the preset sampling depth, the host computer sends a control command to the guiding mechanism, which drives the soil-drilling mechanism downward along the guide rail. The downward feed speed can be adjusted within 0.1–5 cm/s.

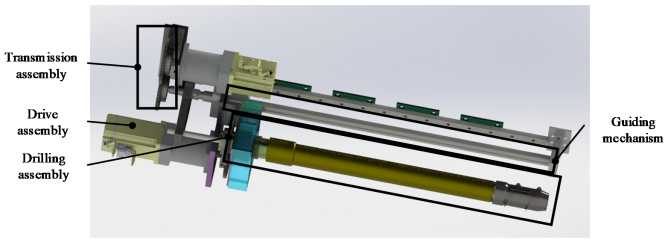

Figure 1. Schematic diagram of the soil-drilling mechanism.

2.2 Helical Soil-Conveying Mechanism and Flight Parameter Design

The soil-drilling mechanism moves downward under the actuation of the guiding mechanism while the drill bit rotates to penetrate and cut the soil. The soil cut by the drill bit enters the helical conveying section through the contact interface between the bit and the soil at the bottom of the borehole, and is then transported upward by the pushing action of the soil below.

At relatively low rotational speeds, the soil is gradually conveyed from the bottom of the borehole toward the ground surface. The helix angle directly affects soil-conveying performance. When the helix angle is too large, approaching 30°, soil tends to slide down along the flight, which makes conveying unstable or inefficient. When it is too small, approaching 8°, the resistance to soil transport increases, which may cause blockage or require a higher rotational speed to maintain conveying. A helix angle between 8° and 30° is therefore generally selected. Considering these two effects, the helix angle of the flight was set to 14°. The pitch follows from the helix angle and the diameter of the helical shaft:

$$\beta = \arctan \frac{S}{\pi D}, \tag{1}$$

where β is the helix angle, S is the pitch, and D is the diameter of the helical shaft.

The calculated pitch is approximately 35 mm. Studies of tube-sampler design show that tube geometry governs sample disturbance [16], and DEM studies of drilling tools with helical flights can be used to analyze the migration and accumulation of material within the helical groove [17]. The auger parameters should therefore be considered together with the drilling operating conditions analyzed later.

2.3 Drill-Bit Structural Design

Many studies have investigated the mechanics of soil cutting by tools through experimental and numerical approaches. Among analytical approaches, the two- and three-dimensional cutting models proposed by McKyes and Ali [18] from basic soil mechanics, referred to here as the McKyes-Ali model, are among the most representative. The model reduces the tool-soil interaction to a mechanical equilibrium problem and has been widely used to describe cutting in soft soils. Many later models modify or extend it.

However, the conventional McKyes-Ali model simplifies the shear failure surface of the soil to a

single plane, which does not represent the complex failure observed when cutting soft soil. To describe soft-soil cutting more accurately, Shen et al. [14] developed a three-dimensional mechanical model within the McKyes-Ali framework by incorporating Rankine passive earth pressure theory and the Mohr-Coulomb yield criterion. The failure surface is represented as a composite slip surface consisting of a planar surface and a logarithmic spiral surface. Before the mechanical model is set up, the cutting angles of the tool are defined, as shown in Figure 2. The tool geometry is characterized by the rake angle ε and the clearance angle α. Both angles are typically selected within $5°$-$20°$, depending on the soil being cut.

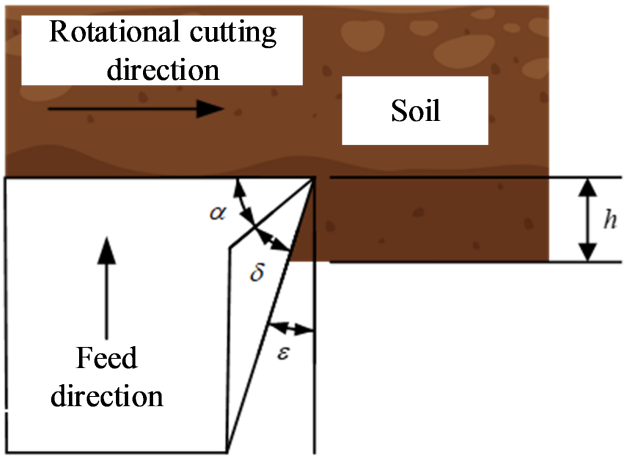

Figure 2. Tool cutting angles.

The three-dimensional mechanical model is illustrated in Figure 3. The logarithmic spiral surface gives a closer representation of the plastic flow of soil and a more useful basis for optimizing drill-bit thrust force and drilling torque. Based on the Mohr-Coulomb failure criterion, Godwin and Spoor showed that the ratio of working depth to tool width for narrow tools affects the soil failure mode, and that the critical cutting depth and horizontal cutting force can be estimated from soil properties and tool geometry, which allows the drill-tip width to be matched to the cutting depth [19].

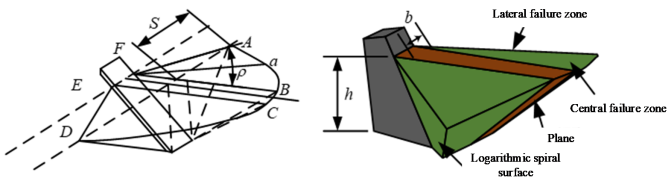

Figure 3. Three-dimensional force model for soil cutting.

On this basis, the three-dimensional force model developed here consists of three regions: one central failure zone and two lateral failure zones on either side of the cutting tool. The lateral failure zones are the soil regions on both sides of the tool that heave laterally and fail under compression, forming approximately ear-shaped or crescent-shaped regions in three-dimensional space. To integrate the forces acting in these regions, a local coordinate system is established and the key geometric parameters are defined. The forces acting on the central failure zone are shown in Figure 4, where the gravitational force is resolved into tangential and radial components.

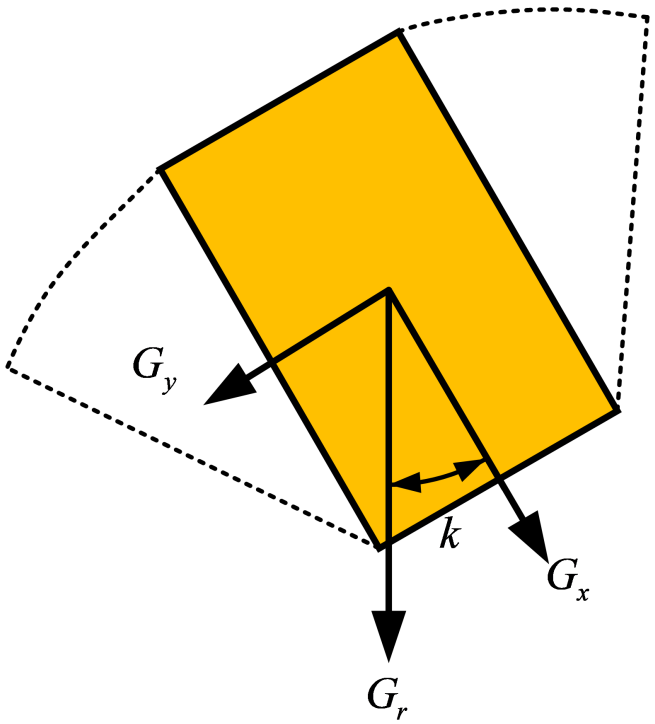

Figure 4. Decomposition of the gravitational force acting on the central soil wedge.

The central failure zone is the soil region directly in front of the cutting tool, with a width approximately equal to the tool width b. During cutting, the soil in this region is compressed by the tool face, fails in shear, and moves upward along the slip surface. Let the rotational angle of the cutter head be k, measured from the vertical axis, and let the total weight of the cut soil be G_γ. Following Shen et al. [14], the gravitational force is resolved into components along the tangential cutting direction (x axis) and the radial direction (y axis):

$$G_x = G_\gamma \cos k, \tag{2}$$

$$G_y = G_\gamma \sin k. \tag{3}$$

The geometric boundaries of the lateral failure zones follow from the model assumptions given below. According to the Mohr-Coulomb yield criterion, the

slip surface under passive earth pressure conditions is not a single plane. In the present model, the slip surface of the central failure zone consists of two parts, as shown in Figure 5.

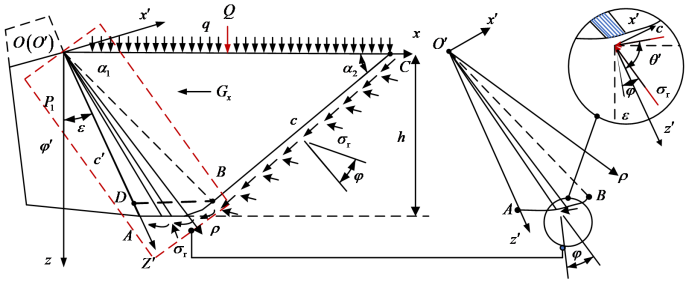

Figure 5. Schematic diagram of forces acting on the central failure zone.

The straight segment BC represents the region away from the cutter tip, where the soil reaches the Rankine passive limit state. The logarithmic spiral segment AB forms a transition zone between the cutter tip and the Rankine zone and accounts for the rotation of the principal stresses. The logarithmic spiral is

$$r_e = \overline{OA}\, e^{\theta \tan \phi}, \tag{4}$$

where r_e is the radial coordinate, θ is the polar angle, and ϕ is the internal friction angle of the soil.

This geometry ensures that the line of action of the resultant force at every point along the slip surface passes through the center of the spiral, which removes the moment of the unknown reaction force from the moment-equilibrium analysis. The angle α_2 defining the Rankine zone follows from classical soil mechanics:

$$\alpha_2 = \frac{\pi}{4} - \frac{\phi}{2}. \tag{5}$$

To determine the reaction force P_1 exerted by the soil on the cutting tool, the forces on the straight segment BC and the curved segment AB are analyzed separately. Let σ_r denote the reaction force per unit area along the slip surface. The resultant reaction force R_1 along BC is resolved into horizontal (R_{1h}) and vertical (R_{1v}) components:

$$\begin{aligned} R_{1h} &= \sigma_r b\, \overline{BC} \sin(\alpha_2 + \phi), \\ R_{1v} &= \sigma_r b\, \overline{BC} \cos(\alpha_2 + \phi). \end{aligned} \tag{6}$$

The resistance components due to the cohesion c along the slip surface are

$$\begin{aligned} C_{1h} &= cb\, \overline{BC} \cos \alpha_2, \\ C_{1v} &= cb\, \overline{BC} \sin \alpha_2. \end{aligned} \tag{7}$$

The curved segment AB follows a logarithmic spiral, along which the tangential direction of the slip surface varies continuously with the polar angle θ. For an infinitesimal element $\mathrm{d}\theta$, the differential reaction force $\mathrm{d}R_2$ is

$$\begin{aligned} \mathrm{d}R_{2h} &= \sigma_r b r_e\, \mathrm{d}\theta \sin\left(\theta' + \phi - \frac{\pi}{2} + \varepsilon\right), \\ \mathrm{d}R_{2v} &= \sigma_r b r_e\, \mathrm{d}\theta \cos\left(\theta' + \phi - \frac{\pi}{2} + \varepsilon\right), \end{aligned} \tag{8}$$

where θ' is the angle of the tangent to the logarithmic spiral at the point considered.

Because θ' has a complex geometrical relationship with θ, the total reaction force R_2 must be evaluated by integration. The upper integration limit α_3, which defines the angular extent of the spiral, follows from the boundary-continuity condition that the tangent slope of the spiral at point B equals the slope of the straight segment BC. Numerical integration gives the horizontal and vertical components of the total reaction force along the curved segment, R_{2h} and R_{2v}, and the corresponding cohesion contributions, C_{2h} and C_{2v}.

Static-equilibrium equations are then written for the entire central failure wedge, including the cutting-tool thrust P_1, the interface friction angle ϕ', the interface cohesion c', the soil self-weight contribution G_x, and the additional force Q induced by the overburden pressure. The horizontal force-equilibrium equation $\sum F_x = 0$ is

$$\begin{aligned} P_1 \sin\left(\frac{\pi}{2} - \varepsilon + \phi'\right) + c' hb \cot\left(\frac{\pi}{2} - \varepsilon\right) \\ - R_{1h} - R_{2h} - C_{1h} - C_{2h} - G_x = 0. \end{aligned} \tag{9}$$

The vertical force-equilibrium equation $\sum F_z = 0$ is

$$\begin{aligned} - P_1 \cos\left(\frac{\pi}{2} - \varepsilon + \phi'\right) + c' hb \\ - R_{1v} - R_{2v} + C_{1v} + C_{2v} + Q = 0. \end{aligned} \tag{10}$$

Solving them simultaneously and eliminating the unknown internal-stress term gives the cutting resistance of the central failure zone:

$$\begin{aligned} P_1 = \frac{A_2 \left(c' hb \tan \varepsilon - C_{1h} - C_{2h} - G_x\right)}{A_1 \sin(\phi' - \varepsilon) - A_2 \cos(\phi' - \varepsilon)} \\ - \frac{A_1 \left(c' hb + C_{1v} + C_{2v} + Q\right)}{A_1 \sin(\phi' - \varepsilon) - A_2 \cos(\phi' - \varepsilon)}, \end{aligned} \tag{11}$$

where h is the cutting depth, i.e., the vertical distance over which the tool penetrates the undisturbed soil; b is the tool width, i.e., the transverse width of the cutting edge; ε is the tool rake angle, i.e., the angle between the

cutting face and the vertical plane; and A_1 and A_2 are the horizontal and vertical reaction-force coefficients of the central failure zone, defined by $R_{1h} + R_{2h} = A_1\sigma_r$ and $R_{1v} + R_{2v} = A_2\sigma_r$, i.e.,

$$A_1 = b\left[\overline{BC}\sin(\alpha_2+\phi) + \overline{OA}\int_0^{\alpha_3} e^{\theta\tan\phi}\sin\left(\theta'+\phi-\frac{\pi}{2}+\varepsilon\right)\mathrm{d}\theta\right],$$
$$A_2 = b\left[\overline{BC}\cos(\alpha_2+\phi) + \overline{OA}\int_0^{\alpha_3} e^{\theta\tan\phi}\cos\left(\theta'+\phi-\frac{\pi}{2}+\varepsilon\right)\mathrm{d}\theta\right].$$

The failure-zone length a (the horizontal projected length of the central failure zone) and the opening angle ρ of the lateral failure zone (its angular extent in the plane perpendicular to the cutting direction) are used in the lateral analysis below.

Equation (11) shows that the cutting resistance P_1 depends on the soil-strength parameters (c, ϕ) and, strongly, on the rake angle ε and the cutting depth h.

The lateral failure zone does not extend indefinitely; its extent is constrained geometrically by the tool dimensions and the cutting depth. According to Shen et al. [14], a strict geometrical relationship exists among the maximum opening angle ρ of the lateral failure zone, the length a of the central failure zone, and the cutting depth h. The cosine of ρ is

$$\cos\rho = \frac{h\cot\left(\frac{\pi}{2}-\varepsilon\right)}{a}. \tag{12}$$

This equation shows that the extent of the lateral failure zone depends on the rake angle, both directly through $\tan\varepsilon$ and indirectly through the length a of the central failure zone. With h and a held constant, increasing ε increases $\cos\rho$, i.e., it reduces the opening angle ρ. The net effect of the rake angle on the lateral disturbance width therefore depends on how fast a changes with ε, and was evaluated numerically below.

The central failure-zone length a is a key geometrical parameter linking the central and lateral failure zones. With the logarithmic-spiral failure mechanism, a can no longer be obtained from a simple trigonometric relationship. Its expression contains an exponential term that accounts for the cumulative stress effects within the spiral field:

$$a = \overline{OB}\cos\left(\frac{\pi}{2}-\varepsilon-\alpha_3\right)\left[1+\tan\left(\frac{\pi}{2}-\varepsilon-\alpha_3\right)\cot\alpha_2\right], \tag{13}$$

where $\overline{OB}$ is the boundary value of the radial coordinate of the spiral, determined by the cutting depth h and the spiral angle α_3:

$$\overline{OB} = \frac{h}{\cos\varepsilon}e^{\alpha_3\tan\phi}. \tag{14}$$

The exponential term $e^{\alpha_3\tan\phi}$ in Eq. (14) is a defining feature of the logarithmic-spiral failure surface. It means that the characteristic length of the failure zone grows exponentially with the internal friction angle ϕ, which indicates that the cutting-induced failure zone tends to be more extensive in soils with a larger internal friction angle.

At an arbitrary opening angle ρ, the tangential width s of the lateral failure zone is

$$s = a\sin\rho. \tag{15}$$

This parameter is used to determine the moment arm and soil volume when integrating over the infinitesimal elements.

To determine the reaction force P_2 exerted by the lateral failure zone on the cutting tool, an infinitesimal-slice method is used. The principal parameters are shown in Figure 6. An infinitesimal soil wedge subtending an angle $\mathrm{d}\rho$ within the lateral failure zone is isolated for free-body analysis. The forces acting on this element are: the tool force $\mathrm{d}P_2$, comprising the normal thrust and friction exerted by the lateral face of the tool; the soil reaction $\mathrm{d}R$, comprising the normal reaction and friction on the sliding failure surface; the cohesive resistance $\mathrm{d}C$ acting tangentially along the sliding surface; the weight $\mathrm{d}G$ of the soil element; and the surcharge force $\mathrm{d}Q$ due to the overlying soil.

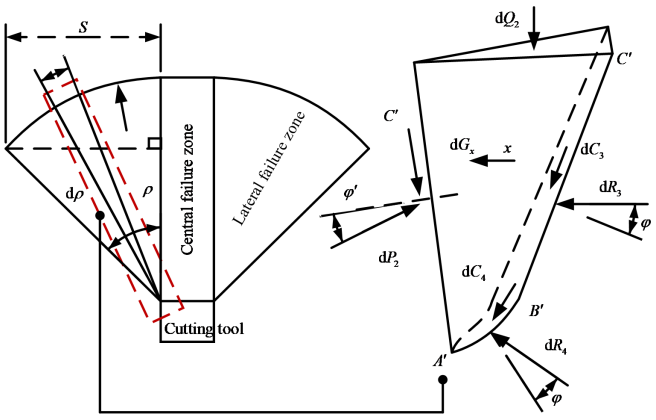

Figure 6. Lateral failure zone and forces acting on an infinitesimal soil element.

Because the model assumes a composite failure surface consisting of the straight segment $B'C'$ and the logarithmic-spiral segment $A'B'$, the stresses over these two segments are integrated separately and the resulting forces are summed. The straight segment $B'C'$ corresponds to the Rankine passive zone, where the stress distribution is relatively uniform. Let $\mathrm{d}R_3$

denote the soil reaction on the straight segment, and let σ_r denote the resultant traction per unit area along the slip surface, comprising the normal and frictional tractions. The differential reaction force $\mathrm{d}R_3$ on $B'C'$ is resolved into horizontal ($\mathrm{d}R_{3h}$) and vertical ($\mathrm{d}R_{3v}$) components. From the geometry, the differential area over which the reaction acts is proportional to the width of the infinitesimal element:

$$\begin{aligned} \mathrm{d}R_{3h} &= \sigma_r \frac{a+\overline{BD}}{2}\,\overline{BC}\sin(\alpha_2+\phi)\,\mathrm{d}\rho, \\ \mathrm{d}R_{3v} &= \sigma_r \frac{a+\overline{BD}}{2}\,\overline{BC}\cos(\alpha_2+\phi)\,\mathrm{d}\rho, \end{aligned} \tag{16}$$

where $(a+\overline{BD})/2$ is the mean radius of the lateral infinitesimal element along segment $B'C'$ and $\overline{BC}$ is the length of the slip line.

The angle $\alpha_2+\phi$ is the inclination of the reaction force relative to the horizontal axis: the internal friction angle ϕ accounts for the resultant reaction force being inclined from the normal to the slip surface by ϕ. The horizontal and vertical cohesion components, $\mathrm{d}C_{3h}$ and $\mathrm{d}C_{3v}$, are

$$\begin{aligned} \mathrm{d}C_{3h} &= c\frac{a+\overline{BD}}{2}\,\overline{BC}\cos\alpha_2\,\mathrm{d}\rho, \\ \mathrm{d}C_{3v} &= c\frac{a+\overline{BD}}{2}\,\overline{BC}\sin\alpha_2\,\mathrm{d}\rho, \end{aligned} \tag{17}$$

where $\overline{BD}$ is an auxiliary geometrical parameter given by

$$\overline{BD} = \frac{\overline{OA}\sin\alpha_3}{\cos\varepsilon}. \tag{18}$$

The curved segment $A'B'$, which connects the cutter tip to the Rankine zone, forms a transition region known as the Prandtl zone. Within this region, the tangential angle of the slip surface varies continuously with the polar angle θ, so the directions of both the reaction force and the cohesive resistance change continuously. Integration coefficients are therefore introduced. Let $\mathrm{d}R_4$ denote the total reaction force along the logarithmic-spiral segment, obtained by integration with respect to θ from 0 to α_3. To simplify the resulting expressions, the coefficients A_3 and A_4 are introduced:

$$\mathrm{d}R_{4h} = A_3\,\overline{OA}^{\,2}\sigma_r\,\mathrm{d}\rho, \tag{19}$$

$$\mathrm{d}R_{4v} = A_4\,\overline{OA}^{\,2}\sigma_r\,\mathrm{d}\rho, \tag{20}$$

where A_3 and A_4 are the horizontal and vertical reaction-force coefficients, respectively:

$$A_3 = \int_0^{\alpha_3} \frac{\sin\theta}{\cos\varepsilon} e^{2\theta\tan\phi}\sin\Big(\theta'+\phi-\frac{\pi}{2}+\varepsilon\Big)\,\mathrm{d}\theta, \tag{21}$$

$$A_4 = \int_0^{\alpha_3} \frac{\sin\theta}{\cos\varepsilon} e^{2\theta\tan\phi}\cos\Big(\theta'+\phi-\frac{\pi}{2}+\varepsilon\Big)\,\mathrm{d}\theta. \tag{22}$$

The term $\overline{OA}^{\,2}$ originates from the squared radial coordinate r_e^2 of the logarithmic spiral. In the moment-equilibrium and surface-area integrations, both the moment arm and the area of application depend on the radial coordinate, which gives rise to the $e^{2\theta\tan\phi}$ term. The force generated within the lateral failure zone is therefore highly sensitive to the internal friction angle ϕ: a small increase in ϕ can substantially increase A_3 and A_4 and hence the cutting resistance. The expression $\theta'+\phi-\pi/2+\varepsilon$ accounts for the reaction force being inclined at an angle ϕ to the normal to the local tangent; θ' is the tangent angle of the spiral and varies with θ, which keeps the mechanical boundary conditions continuous. Let $\mathrm{d}C_4$ denote the cohesive resistance along the curved segment. Its horizontal and vertical components are obtained by integration with the coefficients A_5 and A_6:

$$\mathrm{d}C_{4h} = A_5\,\overline{OA}^{\,2}c\,\mathrm{d}\rho, \tag{23}$$

$$\mathrm{d}C_{4v} = A_6\,\overline{OA}^{\,2}c\,\mathrm{d}\rho. \tag{24}$$

The coefficients A_5 and A_6 are

$$A_5 = \int_0^{\alpha_3} \frac{\sin\theta}{\cos\varepsilon} e^{2\theta\tan\phi}\sin(\pi-\theta'-\varepsilon)\mathrm{d}\theta, \tag{25}$$

$$A_6 = \int_0^{\alpha_3} \frac{\sin\theta}{\cos\varepsilon} e^{2\theta\tan\phi}\cos(\pi-\theta'-\varepsilon)\mathrm{d}\theta. \tag{26}$$

Static-equilibrium equations are written for an infinitesimal element within the lateral failure zone in the horizontal (x) and vertical (z) directions. The element is subjected to the tool force $\mathrm{d}P_2$, the reaction forces ($\mathrm{d}R_3$, $\mathrm{d}R_4$) on the failure surface, the cohesive resistance ($\mathrm{d}C_3$, $\mathrm{d}C_4$), the self-weight $\mathrm{d}G$, and the overburden-induced force $\mathrm{d}Q$. The horizontal equation is

$$\begin{aligned} \mathrm{d}P_2\sin\Big(\frac{\pi}{2}-\varepsilon+\phi'\Big) - \mathrm{d}R_{3h} - \mathrm{d}R_{4h} \\ - \mathrm{d}C_{3h} - \mathrm{d}C_{4h} - \mathrm{d}G = 0. \end{aligned} \tag{27}$$

The vertical equation is

$$\begin{aligned} -\mathrm{d}P_2\cos\Big(\frac{\pi}{2}-\varepsilon+\phi'\Big) - \mathrm{d}R_{3v} - \mathrm{d}R_{4v} \\ + \mathrm{d}C_{3v} + \mathrm{d}C_{4v} + \mathrm{d}Q = 0, \end{aligned} \tag{28}$$

where ϕ' is the interface friction angle between the cutting tool and the soil, and $\mathrm{d}G$ is the weight of the soil element.

To simplify the solution, four composite geometric parameters are introduced to combine the integral and geometrical terms: the total horizontal reaction-force factor B_1, the total vertical reaction-force factor B_2, the total horizontal cohesive-resistance factor B_3, and the total vertical cohesive-resistance factor B_4:

$$B_1 = \frac{a+\overline{BD}}{2}\,\overline{BC}\sin(\alpha_2+\phi) + A_3\overline{OA}^2, \tag{29}$$

$$B_2 = \frac{a+\overline{BD}}{2}\,\overline{BC}\cos(\alpha_2+\phi) + A_4\overline{OA}^2, \tag{30}$$

$$B_3 = \frac{a+\overline{BD}}{2}\,\overline{BC}\cos\alpha_2 + A_5\overline{OA}^2, \tag{31}$$

$$B_4 = \frac{a+\overline{BD}}{2}\,\overline{BC}\sin\alpha_2 + A_6\overline{OA}^2. \tag{32}$$

These factors reduce the formulation to a compact analytical form suitable for engineering calculations and numerical simulation. Solving Eqs. (27) and (28) simultaneously and eliminating the unknown reaction traction σ_r gives the tool force $\mathrm{d}P_2$ on the infinitesimal element:

$$\mathrm{d}P_2 = \frac{B_2B_3+B_1B_4}{K_{\mathrm{denom}}}\,c\,\mathrm{d}\rho + \frac{\frac{1}{2}B_1qa^2}{K_{\mathrm{denom}}}\,\mathrm{d}\rho + \frac{\frac{1}{6}B_2\gamma ha^2\cos(\rho+k)}{K_{\mathrm{denom}}}\,\mathrm{d}\rho, \tag{33}$$

where q is the overburden pressure, γ is the soil unit weight, and the denominator K_{denom} is

$$K_{\mathrm{denom}} = B_2\cos(\phi'-\varepsilon) - B_1\sin(\phi'-\varepsilon). \tag{34}$$

This expression separates the lateral cutting force into three contributions arising from soil cohesion, overburden pressure, and soil self-weight. The total resistance P_2 exerted by the lateral failure zone on the cutting tool is obtained by summing the projections of all differential forces onto the direction of tool advance. Because the lateral failure zone spreads in a fan-shaped pattern, the integration is performed with respect to the opening angle from 0 to ρ:

$$P_2 = \int_0^{\rho}\cos\rho'\,\mathrm{d}P_2. \tag{35}$$

Substituting the expression for $\mathrm{d}P_2$ and evaluating the integral gives the lateral cutting force:

$$P_2 = \frac{B_2B_3+B_1B_4}{K_{\mathrm{denom}}}\,c\sin\rho + \frac{\frac{1}{2}B_1qa^2}{K_{\mathrm{denom}}}\sin\rho + \frac{\frac{1}{24}B_2\gamma ha^2\left[(\sin 2\rho+2\rho)\cos k + (\cos 2\rho-1)\sin k\right]}{K_{\mathrm{denom}}}. \tag{36}$$

The total reaction force on the end face of the cutting tool is therefore

$$P = P_1 + 2P_2. \tag{37}$$

This section derives an analytical expression, $P = P_1 + 2P_2$, for the total cutting resistance acting on the sampling drill under unstructured soil conditions. The model addresses a limitation of the conventional two-dimensional McKyes-Ali theory, which considers only the resistance of the central failure zone and neglects lateral soil extrusion. By adding the resistance generated in the two lateral failure zones, it better reflects the three-dimensional loading of the rotary cutting process. Using this model, MATLAB-based numerical calculations were performed to evaluate the sensitivity of the cutting resistance to the key geometrical parameters of the drill bit and to optimize them. The results identify the rake angle ε as the dominant parameter affecting cutting energy consumption. As ε increases, the central shearing resistance P_1 decreases markedly, whereas the proportion of the lateral resistance P_2 gradually increases because of the change in the geometry of the lateral failure zones. The total cutting resistance P reaches a minimum at the rake angle $\varepsilon = 18°$, which lies within the usual rake-angle range of 5°–20° and was adopted in the final drill-bit configuration. Lateral resistance accounts for approximately 30%–40% of the total cutting load, which shows that a three-dimensional mechanical model is needed. The relationship between total cutting resistance, lateral resistance, and rake angle is shown in Figure 7.

The unit weight of the soil follows from its density:

$$\gamma = \rho_s g = 1758\times 9.8 = 17228.4\,\mathrm{N/m^3} \approx 17.23\,\mathrm{kN/m^3}. \tag{38}$$

The values of c and ϕ were taken from the literature. Based on the soil shear strength specified in China's current Code for Design of Building Foundation (GB 50007-2011), cohesive soil with relatively high shear strength was considered, using 100 kPa for cohesion and 22° for the internal friction angle.

According to the textbook *Agricultural Machinery*, the internal friction angle ranges from 18° to 25° for silt and from 15° to 22° for typical cohesive soils. Silty clay lies between these two soil types; therefore, an internal friction angle of 22° was adopted. The soil-tool interface friction angle ϕ' may be approximated as $\phi' = (0.5 \sim 0.7)\phi$. The relevant parameters are listed in Table 1.

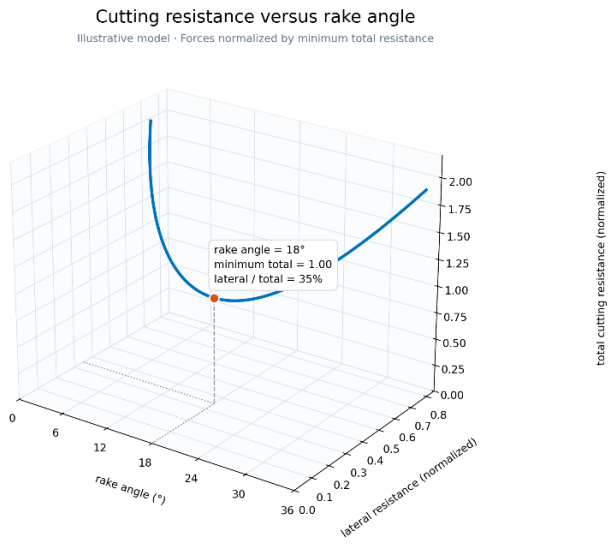

Figure 7. Relationship between total cutting resistance, lateral resistance, and rake angle.

Table 1. The relevant parameters.

Symbol	Parameter name	Value	Unit
c	Soil cohesion	100	kPa
ϕ	Soil internal friction angle	22	°
γ	Soil unit weight	17.23	kN/m^3
ϕ'	Soil-tool interface friction angle	15	°

The soil failure region consists of a central failure zone directly in front of the tool and two lateral failure zones on either side. In the central failure zone, the soil is compressed by the tool face, fails in shear, and moves upward along the slip surface. In the lateral failure zones, the soil is displaced outward by the tool, producing lateral heave and failure. Including lateral failure in the model avoids the underestimation of total cutting resistance that results from considering only the central failure zone.

The main design parameters of the hollow soil-sampling drill tool are the inner diameter of the tube shoe (d_1), the outer diameter of the tube shoe (d_2), the cutting-edge angle of the tube shoe (ϕ), the tube-shoe height (b), the cutting depth of the tube shoe (a), the cutting-edge tip width (l), and the diameter of the central outer tube (D_c) [16]. The structure is shown in Figure 8. These parameters determine the cutting performance and sampling quality and directly affect drilling resistance and sample integrity.

During soil sampling, friction between the soil sample and the inner wall of the drill tool can disturb the outer portion of the sample, and the

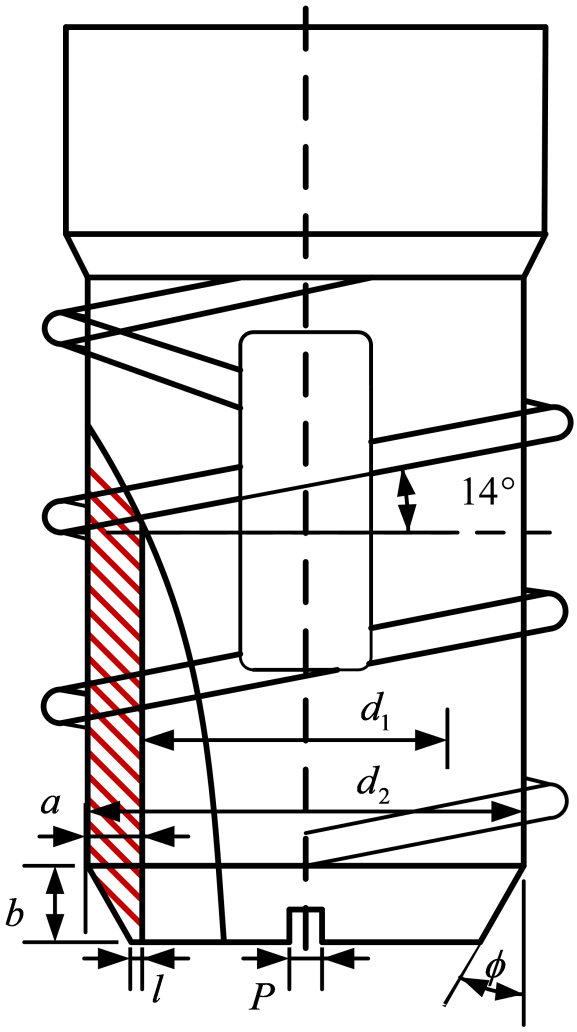

Figure 8. Key design parameters of the drilling tool.

extent of this disturbance is strongly related to the wall thickness of the sampling tool. In general, reducing the wall thickness decreases both sample disturbance and drilling resistance. An excessively thin wall may, however, deform or fail during drilling, which compromises sampling accuracy and structural reliability. Numerical and analytical studies of tube sampling show that sampler geometry, including wall thickness, governs sample disturbance [16], so a thinner wall is preferred. Considering sample disturbance, structural strength, and manufacturing requirements, the wall thickness of the drill tool was set to 4 mm.

The key operating principle of the soil-drilling mechanism is to cut the soil in the central region with the drill bit and guide it toward the surrounding area, which facilitates soil transport. A tube-shoe angle of 15° was adopted. A smaller angle lowers the penetration resistance but weakens the cutting

edge, whereas a larger angle raises the resistance and the disturbance of the sample, so 15° was chosen as a compromise. The tube-shoe height should not be too large, because a tall tube shoe increases the frictional resistance on the soil sample passing through it and may degrade sampling quality. An appropriate tube-shoe height generally ranges from 15 to 30 mm. Considering drilling resistance and structural size constraints, the tube-shoe height was set to 15 mm.

3 Drill-Bit Structural Simulation

This section investigates the dynamic behavior of the drill bit during soil sampling. As the component through which the sampling device interacts with the soil, the mechanical response of the drill bit directly affects sampling efficiency and sample integrity. Because soil exhibits nonlinear, granular, and strongly coupled mechanical behavior, conventional theoretical models and simplified analytical methods often cannot represent actual operating conditions. EDEM predictions are highly sensitive to model parameters, and some particle-scale parameters cannot be measured directly, so parameter calibration is needed to ensure that the simulated particle behavior represents that of the actual soil [20]. A coupled RecurDyn-EDEM simulation was therefore adopted to analyze the forces on the drill bit, its motion, and soil flow. A discrete element model of the soil was established first, followed by analysis of the mechanical response of the drill bit. DEM has been used to analyze material conveying in drilling tools with helical flights [17]. Comparing simulation results under different operating conditions shows the effects of drill-bit geometry, rotational speed, and feed speed on the mechanical response and sampling performance, which provides a basis for structural optimization and parameter selection.

Natural soil particles generally have complex morphologies. In discrete element modeling of soil-tool interaction, the particle representation, contact model, and contact parameters determine the predicted macroscopic behavior and tool forces [21], so equivalent particle assemblies are used to reproduce the macroscopic properties of soil. Three representative particle morphologies were generated by combining spherical particles into columnar, core-like, and block-like agglomerates. During co-simulation, RecurDyn transfers the displacement and velocity of the drill bit to EDEM, while EDEM calculates the particle-structure contact forces and returns them to the multibody dynamics model, which gives two-way coupling between drill-bit motion and the response of the soil particles. Considering computational efficiency and the macroscopic mechanical behavior of the soil, a block-like particle assembly composed of spherical particles was adopted for the drilling simulations. The coordinate parameters are listed in Table 2.

Considering the interparticle adhesion of silty clay, the Hertz-Mindlin with JKRV2 contact model was adopted for contact between soil particles [22]. The intrinsic material properties of the soil and steel, including density, Poisson's ratio, and shear modulus, were taken from previous studies, while the particle contact parameters were obtained by calibration. The parameter set that minimized the discrepancy between simulated and measured results was selected, as listed in Table 3. It serves as input for the simulation of soil-tool interaction and for analyzing the failure and flow of soil particles during drill-bit penetration.

The calibration target was a natural angle of repose of 30.1°, following the angle-of-repose calibration approach of Roessler and Katterfeld [23]. An orthogonal experimental design was then used to evaluate the effects of the coefficient of restitution, coefficient of static friction, and coefficient of rolling friction on the particle accumulation pattern. The intrinsic properties of the soil and steel, together with the ranges of the contact parameters, were set according to relevant discrete element studies.

A naturally settled particle bed of $200 \times 200 \times 450$ mm was used to represent the soil domain; its layered structure is shown in Figure 9(a). For the initial drilling condition, the drill bit was placed above the particle bed with a rotational speed of 15 rad/s (approximately 143 r/min) and a feed speed of 30 mm/s. As the bit began to rotate and advance downward, the soil particles were progressively disturbed and displaced under gravity and interparticle contact forces. After 3.4 s of simulation, the drill bit had partially penetrated the particle bed, as shown in Figure 9(b).

To characterize the mechanical response of the drill bit under different operating conditions and to optimize the operating parameters for several objectives, response surface experiments were conducted using a central composite rotatable response surface methodology (CCR-RSM) with two factors at five levels. Rotational speed (A) and feed speed (B) were the independent variables, and thrust force (Y_1) and torque about the vertical axis (Y_2) were the response

Table 2. Soil particle parameters.

Particle model	Particle No.	Radius/mm	Contact radius/mm	Particle coordinates (X, Y, Z)/mm
Columnar particle assembly	Particle 1	1	1.2	(0, 0, 0)
	Particle 2	1	1.2	(0, 0.6, 0)
	Particle 3	1	1.2	(0, 0, 0.6)
	Particle 4	1	1.2	(0, 0.6, 0.6)
	Particle 5	1	1.2	(0, 0, 1.2)
Core-like particle assembly	Particle 1	1	1.2	(0, 0, 0)
	Particle 2	1	1.2	(0, 0.8, 0)
	Particle 3	1	1.2	(0, 1.2, 0)
Block-like particle assembly	Particle 1	1	1.2	(0, 0, 0)
	Particle 2	1	1.2	(0.4, 0.4, 0)
	Particle 3	1	1.2	$(-0.4, 0.4, 0)$
	Particle 4	1	1.2	(0.2, 0.3, 0.5)

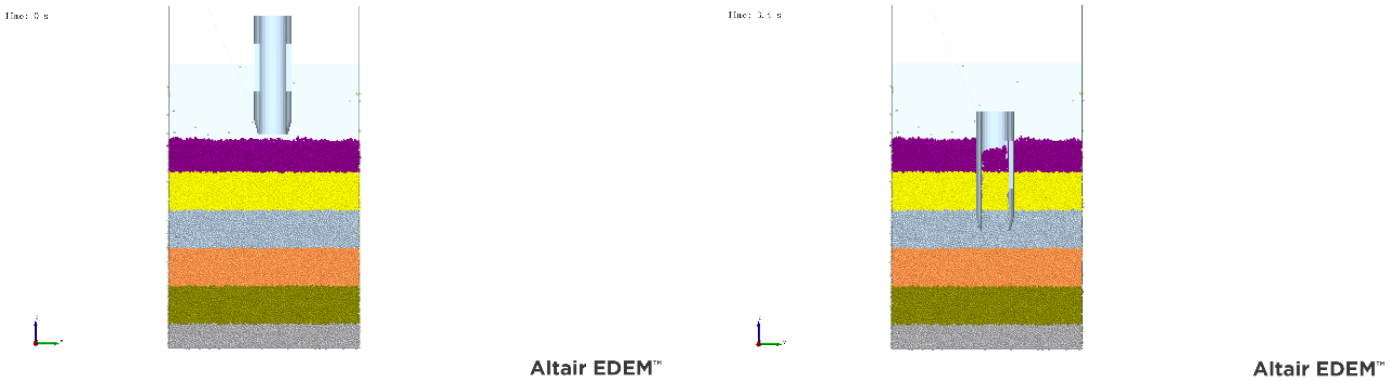

(a) (b)

Figure 9. Simulation of the drilling process: (a) soil stratification; (b) cross-sectional view of the drilling process.

Table 3. Simulation parameters for the soil test.

Parameter	Value
Soil density/(kg/m^3)	1758
Soil Poisson's ratio	0.4
Soil shear modulus/MPa	1
Steel density/(kg/m^3)	7830
Steel Poisson's ratio	0.35
Steel shear modulus/GPa	79
Soil-soil coefficient of restitution	0.53
Soil-soil coefficient of static friction	0.75
Soil-soil coefficient of rolling friction	0.11
Soil-steel coefficient of restitution	0.6
Soil-steel coefficient of static friction	0.51
Soil-steel coefficient of rolling friction	0.05
Soil-soil JKR surface energy/(J/m^2)	2.38

variables.

Based on the operating conditions above, the center-point levels were set to $A_0 = 300$ r/min and $B_0 = 20$ mm/s, with step sizes of 100 r/min and 10 mm/s, respectively. The axial distance was set to 1.414 to ensure rotatability of the design. A total of 13 runs were constructed, comprising four factorial points, four axial points, and five center points. The factor levels, experimental design, and results are given in Table 4, and the analysis of variance in Table 5. The experiments allow the individual and interaction effects of rotational speed and feed speed on the drilling response to be evaluated. Response models relating rotational speed and feed speed to thrust force and torque were then established, which supports the choice of drilling parameters. The regression equations were fitted by multiple regression analysis.

The experimental data were fitted by multiple quadratic regression in Design-Expert. The regression equations for axial thrust Y_1 and torque Y_2 about the vertical axis, expressed in terms of the coded factors A and B, are

$$\begin{aligned} Y_1 &= 145.36 - 6.66A + 63.33B - 1.43A^2 - 0.18B^2 \\ &\quad - 1.25AB, \\ Y_2 &= 15.06 - 0.72A + 6.86B - 0.06A^2 - 0.005B^2 \\ &\quad - 0.20AB. \end{aligned} \tag{39}$$

Table 4. CCR-RSM factor levels, experimental design, and results.

Run No.	A - Rotational speed/(r/min)	B - Feed speed/(mm/s)	Y_1 - Thrust force/N	Y_2 - Torque about the vertical axis/(N·m)
1	200(−1)	10(−1)	85.0	8.5
2	200(−1)	30(+1)	210.0	22.0
3	400(+1)	10(−1)	75.0	7.8
4	400(+1)	30(+1)	195.0	20.5
5	158.6(−1.414)	20(0)	155.0	16.5
6	441.4(+1.414)	20(0)	135.0	14.0
7	300(0)	5.9(−1.414)	55.0	5.2
8	300(0)	34.1(+1.414)	240.0	25.5
9	300(0)	20(0)	145.0	15.4
10	300(0)	20(0)	145.0	15.2
11	300(0)	20(0)	146.0	14.8
12	300(0)	20(0)	145.2	14.9
13	300(0)	20(0)	145.6	15.0

Table 5. Results of the analysis of variance for thrust force Y_1.

Source	Sum of squares	Degrees of freedom	Mean square	F-value	p-value	Significance
Model	32 459.56	5	6 491.91	524.33	< 0.0001	Highly significant
A - Rotational speed	354.90	1	354.90	28.66	0.0011	Significant
B - Feed speed	32 084.18	1	32 084.18	2 591.31	< 0.0001	Highly significant
AB	6.25	1	6.25	0.50	0.500	Not significant
A^2	14.23	1	14.23	1.15	0.319	Not significant
B^2	0.23	1	0.23	0.02	0.895	Not significant
Residual	86.67	7	12.38			
Lack of fit	85.92	3	28.64	152.34	0.0001	Significant
Pure error	0.752	4	0.188			
Total	32 546.23	12				

Feed speed has by far the largest effect on both responses, rotational speed has a smaller but significant effect on thrust force, and the interaction and quadratic terms are not significant. The lack of fit is significant, so the models are used to describe trends within the tested range rather than for precise prediction. Within the tested range, the lowest thrust force and torque occurred at high rotational speed and low feed speed (for example, 400 r/min and 10 mm/s gave 75.0 N and 7.8 N·m), and the feed speed should be chosen as a compromise between drilling load and sampling time.

4 Experiments

The experiment was conducted in an outdoor nursery test area; the prototype is shown in Figure 10. The test site was relatively flat and consisted mainly of silty clay, with sparse weeds on the ground surface. These conditions represent an unstructured outdoor environment, as shown in Figure 11. The weather was clear with good illumination, which met the operating requirements of the onboard LiDAR and vision sensors of the mobile platform.



Figure 10. Photograph of the drilling tool.

The automated soil-sampling device was first mounted on a quadruped robotic mobile platform. The operating route was predefined on a remote host computer, and nine target locations with different

Table 6. Field test results.

No.	Soil depth range/cm	Sampling time/s	Sampling time error/%	Sample mass/g	Sample mass error/%
1	5–10	30.1	1.6	202	1.0
2	5–10	29.8	0.6	204	2.0
3	5–10	30.0	1.3	210	5.0
4	10–15	32.2	1.8	198	1.0
5	10–15	33.0	4.4	207	3.5
6	10–15	32.8	3.7	210	5.0
7	15–20	35.6	5.9	214	7.0
8	15–20	35.8	6.5	212	6.0
9	15–20	36.0	7.1	220	10.0
10	20–30	39.4	8.5	224	12.0
11	20–30	40.8	10.2	229	14.5
12	20–30	41.5	12.6	230	15.0



Figure 11. Field test.

geographic coordinates in the test field were selected as sampling points. After the experiment was started, the quadruped robot received the control commands and navigated autonomously to each target point. After positioning and adjustment to a stable stationary posture, the sampling device was switched from its stowed configuration to the vertical operating configuration. The electric cylinder then drove the drill bit into the soil to the preset depth for depth-specific sampling. After each sample was collected, the system ejected the cylindrical soil core into the collection mechanism and recorded the corresponding information in the RFID tag. This procedure was repeated until automated sampling at all target locations was completed. Samples from four depth intervals, 12 sampling operations in total, were weighed; the measured data and errors are presented in Table 6.

At a sampling depth of 5–10 cm, the sampling-time error remained below 2%. When the soil depth increased to 20–30 cm, it rose to 8.5%–12.6%. This suggests that soil resistance or environmental disturbance becomes more uncertain with depth, which makes sampling times less consistent. The error in sample mass also increased with soil depth. Both the sampling-time error and the sample-mass error therefore grew progressively with sampling depth.

5 Conclusion

A lightweight sampling mechanism based on helical drilling was developed, with attention to drill-bit structural design and mechanical analysis for automated soil sampling. An EDEM model was established to simulate the interaction between the soil and the soil-engaging components. Using a natural angle of repose of 30.1° as the calibration target, the soil contact parameters were calibrated by angle-of-repose simulations and orthogonal parameter tests. With the calibrated model, the mechanical response of the drill bit during soil cutting was analyzed numerically, which supports drill-bit structural design and optimization of the sampling mechanism. Prototype sampling tests were then carried out in an outdoor nursery to evaluate the practical performance of the device. The sampling device collected soil samples at the specified depths. The main conclusions are as follows:

(1) The key structural parameters of the drill bit were determined from the mechanisms of helical soil conveying and three-dimensional soil cutting. The helix angle of the auger flight was set to 14° and the pitch was approximately 35 mm. Calculations with the three-dimensional cutting model showed that the total cutting resistance was lowest at a rake angle of 18°. The resistance of the lateral failure zones accounted for approximately 30%–40% of the total load, so lateral soil failure should not be neglected in the force analysis of the drill bit. Considering sample disturbance, structural strength, and manufacturing requirements, the wall thickness, tube-shoe angle, and tube-shoe height were set to 4 mm, 15°, and 15 mm, respectively.

(2) A discrete element model of the soil was established using the Hertz-Mindlin with JKRV2

contact model, and the contact parameters were calibrated against a target natural angle of repose of 30.1°. Based on the calibrated model, a bidirectionally coupled RecurDyn-EDEM model was developed. A 13-run central composite response surface design was used to investigate the effects of rotational speed and feed speed on the axial force and torque of the drill bit. Feed speed was the dominant factor affecting axial force: increasing it from 10 to 30 mm/s produced a pronounced rise in axial force, whereas a higher rotational speed combined with a lower feed speed facilitated soil discharge and reduced cutting torque. These findings give a basis for selecting drilling parameters and sizing the drive components.

(3) Outdoor sampling tests in silty clay were conducted to verify the performance of the drill bit and sampling mechanism. Twelve sampling tests were completed across four depth intervals ranging from 5 to 30 cm. Nine tests were conducted within the target depth of 10–30 cm, and eight of these yielded samples of at least 200 g. For the 5–10 cm layer, the sampling-time error did not exceed 2%. As sampling depth increased, both the sampling-time error and the sample-mass error generally increased. For the 20–30 cm layer, the two errors ranged from 8.5% to 12.6% and from 12.0% to 15.0%, respectively. Operating conditions for deeper sampling remain a priority for further parameter optimization.

Data Availability Statement

Data will be made available on request.

Funding

This work was supported in part by the S&T Program of Hebei under Grant 23315401D; and in part by the Science and Technology Support Project for the New Round of the Strategic Action for Mineral Exploration Breakthroughs under Grant ZKKJ202625.

Conflicts of Interest

The authors declare no conflicts of interest.

AI Use Statement

The authors declare that no generative AI was used in the preparation of this manuscript.

Ethical Approval and Consent to Participate

Not applicable.

References

[1] Norby, J., Wang, S., Wang, H., Deng, S., Jones, N., Mishra, A., ... & Lowry, G. V. (2024). Path to autonomous soil sampling and analysis by ground-based robots. *Journal of Environmental Management, 360*, 121130. [CrossRef]

[2] Harper, H. J. (1931). An improved soil sampling tube. *Soil Science, 32*(1), 65-70. [CrossRef]

[3] Groenewoud, H. van. (1960). Methods and samplers for obtaining undisturbed soil samples in the forest. *Soil Science, 90*(5), 272-274. [CrossRef]

[4] Walker, M. E., Stansell, J. R., & Shannon, J. E. (1976). Precision soil sampler. *Agronomy Journal, 68*(2), 431-432. [CrossRef]

[5] Karahashi, M., Morimoto, K., Goto, T., & Fujii, Y. (1987). Development of a new soil-core sampler. *Japan Agricultural Research Quarterly, 21*(1), 28-35. https://www.jircas.go.jp/sites/default/files/publication/jarq/21-1-028-035_0.pdf

[6] McGrath, D., & Skotnikov, A. (1996). Possibility of different soil sampling techniques with automated soil sampler. *Communications in Soil Science and Plant Analysis, 27*(5-8), 1779-1794. [CrossRef]

[7] Burrage, R. H., Vibert, R. O., & MacLeod, M. N. (1963). Note on a power-operated soil sampler for field wireworm studies. *Canadian Journal of Plant Science, 43*(2), 242-243. [CrossRef]

[8] Hubers, E. (2002). *U.S. Patent No. 6,363,803*. Washington, DC: U.S. Patent and Trademark Office. https://patents.google.com/patent/US6363803B1/en

[9] Sibley, K. J., Adsett, J. F., & Struik, P. C. (2008). An on-the-go soil sampler for an automated soil nitrate mapping system. *Transactions of the ASABE, 51*(6), 1895-1904. [CrossRef]

[10] Fiechter, T. (2020). *U.S. Patent No. 10,801,927*. Washington, DC: U.S. Patent and Trademark Office. https://patents.google.com/patent/US10801927B2/en

[11] Baarstad, L. L., Rickman, R. W., Wilkins, D., & Morita, S. (1993). A hydraulic soil sampler providing minimum field plot disruption. *Agronomy Journal, 85*(1), 178-181. [CrossRef]

[12] Kornecki, T. S., Prior, S. A., Runion, G. B., Rogers, H. H., & Erbach, D. C. (2008). Hydraulic core extraction: cutting device for soil–root studies. *Communications in Soil Science and Plant Analysis, 39*(7-8), 1080-1089. [CrossRef]

[13] Yildirim, S., Birrell, S. J., & Hummel, J. W. (2006). Laboratory evaluation of an electro-pneumatic sampling method for real-time soil sensing. *Transactions of the ASABE, 49*(4), 845-850. [CrossRef]

[14] Shen, X., Yuan, D., Wu, J., Qiu, T., Chen, X., Jin, D., & Wu, J. (2025). A novel three-dimensional mechanical model for rotary cutting in soil considering wear status and its experimental verification. *Acta Geotechnica, 20*(4), 1661-1679. [CrossRef]

[15] ISO 18400-102:2017. Soil quality–Sampling–Part 102: Selection and application of sampling techniques. International Organization for Standardization, Geneva. Retrieved from https://www.iso.org/standard/62843.html

[16] Clayton, C. R. I., Siddique, A., & Hopper, R. J. (1998). Effects of sampler design on tube sampling disturbance—numerical and analytical investigations. *Géotechnique, 48*(6), 847-867. [CrossRef]

[17] Fu, L., Wang, K., Hu, B., & Xo, N. V. (2021). Conveying performance of drilling tool of auger miner at different strike angles based on discrete element method. *Powder Technology, 378*, 202-215. [CrossRef]

[18] McKyes, E., & Ali, O. S. (1977). The cutting of soil by narrow blades. *Journal of Terramechanics, 14*(2), 43-58. [CrossRef]

[19] Godwin, R. J., & Spoor, G. (1977). Soil failure with narrow tines. *Journal of Agricultural Engineering Research, 22*(3), 213-228. [CrossRef]

[20] Mak, J., Chen, Y., & Sadek, M. A. (2012). Determining parameters of a discrete element model for soil-tool interaction. *Soil and Tillage Research, 118*, 117-122. [CrossRef]

[21] Ucgul, M., Fielke, J. M., & Saunders, C. (2014). Three-dimensional discrete element modelling of tillage: Determination of a suitable contact model and parameters for a cohesionless soil. *Biosystems Engineering, 121*, 105-117. [CrossRef]

[22] Johnson, K. L., Kendall, K., & Roberts, A. D. (1971). Surface energy and the contact of elastic solids. *Proceedings of the Royal Society of London. A, 324*(1558), 301-313. [CrossRef]

[23] Roessler, T., & Katterfeld, A. (2019). DEM parameter calibration of cohesive bulk materials using a simple angle of repose test. *Particuology, 45*, 105-115. [CrossRef]



Ziming Chen is a professor and doctoral supervisor at Yanshan University and currently serves as Vice Dean of the School of Mechanical Engineering. His research interests include robotics, the design and analysis of parallel mechanisms, and the design of novel parallel machine tools and parallel motion simulators. (Email: chenzm@ysu.edu.cn)



Hongyuan Zhang received his bachelor's degree from Henan University of Technology in 2022 and his master's degree from Yanshan University in 2026. He currently works at the Hebei Special Equipment Supervision and Inspection Institute, specializing in custom machinery design. (Email: 1761782044@qq.com)

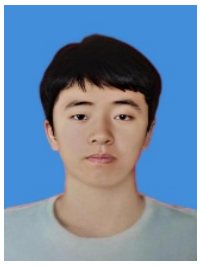

Hongfei Hou received his bachelor's degree from Taiyuan University of Science and Technology in 2025 and is currently pursuing a master's degree at the School of Mechanical Engineering, Yanshan University. (Email: 14735858140@163.com)

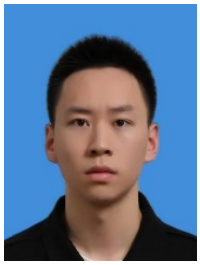

Wang Han received his bachelor's degree from East China University of Science and Technology in 2024 and is currently pursuing a master's degree at the School of Mechanical Engineering, Yanshan University. (Email: 15687024605@163.com)



Pan Zhang received his bachelor's degree from the School of Mechanical Engineering, Luoyang Institute of Science and Technology in 2025 and is currently pursuing a master's degree at Yanshan University. (Email: 2174230972@qq.com)



Wushuai Wang received his bachelor's degree from Qinggong College, North China University of Science and Technology, in 2024. He is currently pursuing a master's degree at the School of Mechanical Engineering, Yanshan University, and is expected to graduate in 2028. (Email: 13290677992@163.com)



Chen Zhao received his Ph.D. from Yanshan University and completed his postdoctoral research at Shanghai Jiao Tong University. He is currently a lecturer at Yanshan University. His research interests include robotics and the design and theory of parallel robots. (Email: zhaochen@ysu.edu.cn)



Qirui Li is an undergraduate student at the School of Electrical Engineering, Yanshan University, with coursework in sensor technology, automatic control, microcontrollers, and C programming. His skills include hardware testing, data processing, and technical feasibility assessment. (Email: qq335445@stumail.ysu.edu.cn)